Received: 19 April 2021 | Revised: 20 July 2021 | Accepted: 3 August 2021

DOI: 10.1002/ima.22648

WILEY

RESEARCH ARTICLE

Approaches to preclinical studies with heterogeneous breast phantom using reconstruction and three-dimensional image processing algorithms for diffuse optical imaging

Yiğit Ali Üncü[1] | Gençay Sevim[2] | Murat Canpolat[1]

[1]Biomedical Optics Research Unit, Department of Biophysics, School of Medicine, Akdeniz University, Antalya, Turkey

[2]Health Services and Techniques, Vocational School of Medical Services, Ufuk University, Ankara, Turkey

Correspondence
Yiğit Ali Üncü, Biomedical Optics Research Unit, Department of Biophysics, School of Medicine, Akdeniz University, Antalya 07058, Turkey.
Email: yuncu@akdeniz.edu.tr

Funding information
Türkiye Bilimsel ve Teknolojik Araştirma Kurumu, Grant/Award Number: 110E263; TUBITAK, Grant/Award Number: 110E263; Akdeniz Üniversitesi, Grant/Award Number: 2009.02.0122.003

Abstract

The continuous-wave back reflection diffuse optical tomography (rCWDOT) system is one of the new medical imaging modalities. This study examines the success of reconstruction and three-dimensional (3D) image processing algorithms on data obtained from a heterogonous breast phantom by rCWDOT. Breast phantoms were prepared by putting a bit of spleen inside the tail. The spleen mimics a breast tumor since it has more blood than tail fat. rCWDOT was used to acquire data from the breast phantoms. The breast phantoms were reconstructed using the transpose-free quasi-minimal residual (TFQMR) reconstruction algorithm. Then, image processing algorithms were performed to improve the image quality. In image processing, 3D Gaussian filtering and bi-cubic interpolation were used to enhance the appearance and remove noise from the images. After the image processing, the images were evaluated numerically using the peak signal-to-noise ratio (PSNR) method. It has been shown that the used reconstruction technique and image processing algorithms for a heterogeneous breast phantom provided 3D images that resemble actual ones. This study will help researchers use the most convenient reconstruction algorithm and image processing algorithms and perform preclinical experiments in this field.

KEYWORDS

3D image processing, bi-cubic interpolation, diffuse optical imaging, Gaussian filtering, transpose-free quasi-minimal residual

1 | INTRODUCTION

Some of the imaging techniques in breast tumor diagnosis are mammography, digital breast tomosynthesis (DBT), positron emission tomography (PET), magnetic resonance imaging (MRI), and ultrasonography (US). Those techniques, including MRI, DBT, mammography, and US, have been used together for breast cancer screening.[1]

Recently, diffuse optical tomography (DOT) has emerged as vital research to image the inside human body and some organs such as the breast and brain.[2–5] DOT aims at producing spatially resolved images based on the blood distribution in tissues and provides[6,7] functional images complementary structural information for MRI scans and X-rays. DOT is a low-cost, portable, and noninvasive imaging technique using a non-ionized

beam.[8,9] DOT also provides information about tissue oxygen saturation using more than one laser wavelength.[10–12] A wavelength ranging between 600 and 1000 nm (near-infrared region) is typically used[7] in DOT. This region is also known as the optical window, and a light having a wavelength in this region has its maximum depth of penetration in the tissue.[7,13]

DOT has been used in several tissue imaging applications for diagnostic purposes.[14,15] DOT system illuminates a tissue through source fibers and detects back- or forward-scattered light from the tissue. The measured data have been used in the solution of the diffusion equation approximated from the radiative light transfer equation (Farrel et al.[16–20]). Fundamentally, the radiative energy transfer (RTE) equation characterizes photons' propagation in the tissue.[10] Therefore, the diffusion approximation of the RTE equation is linearized by either Born or Rytov approximations.[17,21] Several reconstruction algorithms have been used to solve the linearized equation systems in the reconstruction part of DOT in the literature. Also, in our previous studies, several reconstruction algorithms were used in back reflection continuous-wave DOT (rCWDOT) and obtained tomographic images were compared with each other to define which one is the best.[21,22] Studies in the literature show that conjugate gradient (CG)-based reconstruction algorithms become the most effective and quick to solve large, sparse, Hermitian systems.[22–25] However, in our recent study, data acquired from breast phantoms by rCWDOT were reconstructed by transpose-free quasi-minimal residual (TFQMR) and bi-conjugate gradient (BiCG) reconstruction algorithms and it was found that TFQMR has superiority over BiCG in terms of defining correct depth and better spatial resolution.[21]

In general, three-dimensional (3D) filtering methods are recommended to reduce noise in reconstructed images. Filtering is an image processing procedure that performs image smoothing, sharpening, edge detection, enhancement, etc. Generally, smoothing is the corresponding pixel value and neighboring pixels of the input image to determine the image's new pixel (or voxel) value. The most commonly used smoothing filtering method is Gaussian filtering (3D) in the literature,[26] which is used in this study.

In medical imaging, the images should be needed to be enlarged and/or resized without distortion. In 3D images, the possible changes in appearance depending on the acquisition and analysis of images in different angles and directions (x–y, x–z, x–y–z) should not appear. Among the interpolation techniques, bi-cubic interpolation is widely used in 2D and 3D images to resize the image without geometric distortion.[27,28] The proposed algorithms were 3D Gaussian filtering and bi-cubic interpolation algorithms, which increased the image quality in our study.

The effects of image processing algorithms on image quality can be evaluated in two ways: subjective (visual) and objective (numerical). The subjective evaluation is a visual assessment of the image by comparing the images before and after image processing, which is individual-dependent. In numerical evaluation, measurement methods based on specific mathematical models are used. Since the results in mathematical methods mean the same thing for everyone, it is more suitable for measuring image quality and evaluating the algorithm's success. The peak signal-to-noise ratio (PSNR) method, which has been widely used in the literature for the numerical evaluation of image processing algorithms, has the best performance in assessing the quality of noisy images.[29–32]

The reported rCWDOT phantom studies with homogenous structures do not represent the actual breast tissue. We have used tail fat to mimic the breast tissue and spleen to characterize the tumor in obtaining a more realistic heterogeneous breast tissue phantom. In the presented study, rCWDOT data were acquired from the heterogeneous breast phantom, and the TFQMR algorithm reconstructed the breast phantom. Then, 3D Gaussian filtering and bi-cubic interpolation algorithms were applied to increase the image quality.

2 | MATERIALS AND METHODS

2.1 | Heterogeneous breast tissue phantoms' preparation and rCWDOT data acquisition

We bought the tail fat and spleen from a local butcher and kept the tail fat at room temperature for 20 min to soften it. Spleen's depth was measured from the top surface of the fat to the middle of the spleen using a caliper. After data acquisition from the breast phantoms using the rCWDOT, the phantoms were cut to measure the inclusion (spleen) of the depth inside the tail fat. An image of the breast phantom made of tail fat and spleen is shown in Figure 1(A).

The rCWDOT was used to acquire data from the breast phantom. The rCWDOT delivers laser light with a wavelength of 808 nm to the breast phantom using 49 optical fibers, detects diffuse back-reflected light by 49 optical fibers, and sends to photodiodes as described for a schematic presentation in Figure 1(B). The surface area of the optical probe was 28×28 mm^2, and the distance between the closest source and detector was 3 mm. There were 49 source fibers and 49 detector fibers with a diameter of 1 mm on the probe. These fibers' ends were

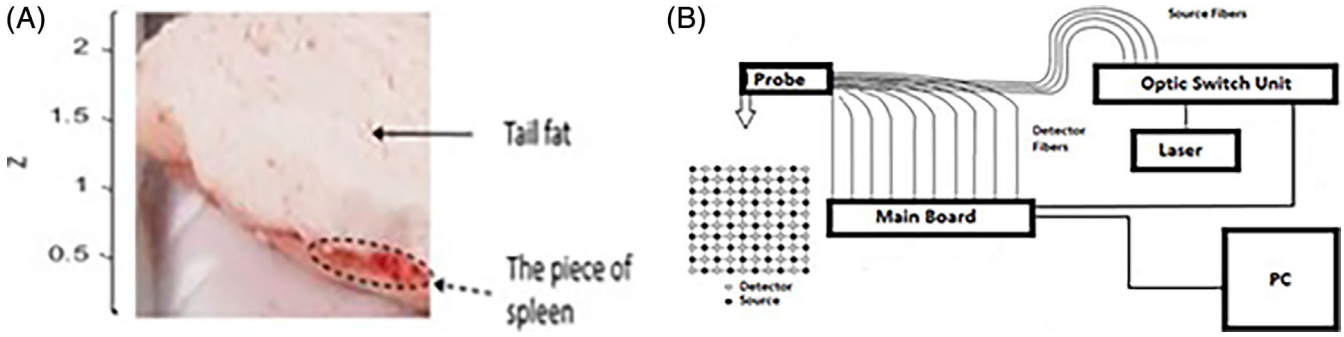

FIGURE 1 (A) The phantom was prepared by placing a bit of spleens as tumor-relevant similar structure into the tail fat to obtain a more realistic breast phantom. (B) Schematic presentation of the rCWDOT system

located on the probe surface in 10 × 10 matrices. There were 22 different source–detector distances and a total of 2401 (49 × 49) matches in the structure of the probe. The distance between the farthest neighbors on the probe was 36.12 mm.[33–35] The rCWDOT measurements were performed by placing the optical probe on the breast tissue phantom. The first measurement was acquired for calibration purposes from the tail fat without the spleen inside it. A bit of the spleen was then placed in different depths of the tail fat.

2.2 | Reconstruction and image processing algorithms

The distribution of light within the tissue characterized by RTE is approximated to the diffusion equation.[20] Then, some approximations such as Rytov were used to create a linear equation system and solve it.[18,21] This linear form is defined as a forward problem (Equation 1) and must be solved as an inverse problem (Equation 2) to create a tomographic image in rCWDOT.

$$y = Ax, \tag{1}$$

$$x = A^{-1}y, \tag{2}$$

y is a measurement perturbation data defined as $y = \log M_h - \log M_p$, where M_h and M_p were rCWDOT data acquired from homogenous tail fat and the tail fat with a spleen inside it, respectively. A is the coefficients' matrix,[34] and x is the matrix of unknowns and represents the distribution of absorption inside the breast phantom. Several reconstruction algorithms solve the inverse problem (Equation 1); however, the TFQMR algorithm was used in this study. Our previous study showed that the TFQMR algorithm provides better tomographic images than BiCG does.[21]

In the quasi-minimal residual method, the non-symmetric Lanczos-based method produces two sequences of vectors as shown in Equations (4) and (5). Sequences in Equation (5) require matrix–vector multiplication.[36,37] Standard QMR uses S, a nonsingular matrix used to simplify the Lanczos process (Equation 3). This simplification provides the elimination of transpose in TFQMR by determining starting vector w_1 (Equationa 6 and, 7).

The TFQMR also uses v_n and w_n Krylov subspace vectors in the solution.[21,36,37] However, the TFQMR method can solve the problem using other matrices instead of A and S in Equation (3), and it converges by changing vector sequences of the conjugate gradient squared (CGS).[36,37] Therefore, this convergence provides low computational cost and smooth convergence.[21,36,37]

$$A^T S = SA, \quad S \in \mathbb{C}^{N\times N}, \quad v_1, w_1 \in \mathbb{C}^N, \tag{3}$$

$$\text{span}\{v_1, v_2, ..., v_n\} = K_n(v_1, A) \quad n = 1, 2, ..., \tag{4}$$

$$\text{span}\{w_1, w_2, ..., w_n\} = K_n\left(w_1, A^T\right) \quad n = 1, 2, ..., \tag{5}$$

v_1 and w_1 are initial the vectors for the solution,

$$w_1 := \frac{1}{\| Sv_1 \|} Sv_1, \tag{6}$$

$$w_n = \frac{\gamma_n}{\| Sv_1 \|} Sv_n = \frac{1}{\| Sv_n \|} Sv_n. \tag{7}$$

In image processing, the first step is to reconstruct the image via the TFQMR method, and the second step is 3D Gaussian filtering to smooth the images. The last step is a 3D interpolation, which performs bi-cubic spline interpolation. The flowchart of the proposed algorithms is shown in Figure 2.

Figure 3 shows an example of raw reconstructed phantom tissue images before and after image processing. The dashed line circles the actual location shape of the spleen in the tail (Figure 3). The spleen's correct center coordinates are $x = 1.5$ cm, $y = 1.25$ cm, and $z = 1$ cm, approximately, as shown in Figure 3(A,B). A 3D Gaussian filter with the weighted average over a mask with a $5 \times 5 \times 5$ (windowing) dimension was used to smooth an image. The central pixel has more contribution than others, resulting in noise reduction and edge stabilization. In Equation 8, the Gaussian curve was designed in 3D with the center of (0,0) point and the standard deviation value ($\sigma = 1$). G (x, y, z) is x, y, z coordinates of Gaussian function and computed values for the mask.

$$G(x,y,z) = \frac{1}{\sqrt{2\pi}\sigma^3} \exp\left(-\left(\frac{x^2+y^2+z^2}{2\sigma^2}\right)\right). \quad (8)$$

The 3D Gaussian filter produces a weighted average for each pixel for smoothing on the rCWDOT image (Figure 3(C)). The quality of a processed image also depends on the adapted interpolation method for rCWDOT imaging. In the last step of image processing, interpolation was used in rCWDOT imaging with the bi-cubic interpolation (Figure 3(D)). The interpolated value at a query point was estimated based on a cubic interpolation of the values at neighboring grid points in each respective dimension.

Quantitative criteria are available to measure the performance of image processing algorithms. The most widely used image assessing criterion is PSNR.[29,32] Mean squared error (MSE) is defined as

$$\mathrm{MSE} = \frac{1}{\mathrm{MN}} \sum_{X=0}^{M-1} \sum_{y=0}^{N-1} \|g(x,y) - h(x,y)\|^2, \quad (9)$$

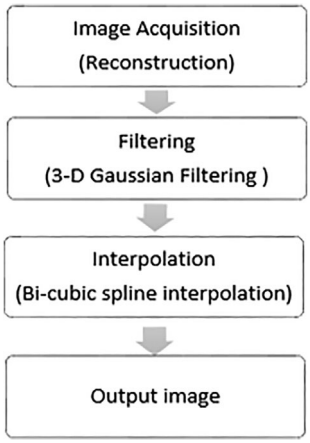

FIGURE 2 Flowchart of the proposed algorithms

where M and N are the image $g(x,y)$ sizes, while $h(x,y)$ is the reconstructed image in Equation 9. The MSE represents the cumulative error of the processed $g(x,y)$ and reconstructed $h(x,y)$ images. PSNR refers to the ratio of the value representing the quality of the distorted signal with the maximum value that the signal can receive. It can be said that the higher the PSNR, the better the image quality. PSNR is often expressed logarithmically since signals in the image have a wide dynamic range.

PSNR is a suitable criterion for noisy images and is defined as

$$\mathrm{PSNR} = 20\log_{10}\left(\frac{\mathrm{Max}_f}{\sqrt{\mathrm{MSE}}}\right), \quad (10)$$

where Max_f represents the maximum pixel intensity of the image in Equation 10. The reconstruction and the image processing algorithms were implemented using MATLAB.

3 | RESULTS

Three-dimensional Gaussian filtering and then the bi-cubic interpolation methods were applied to the image reconstructed by the TFQMR algorithm. The sample dimensions are $39 \times 39 \times 24$ mm^3, the pixel dimensions are $0.26 \times 0.26 \times 0.24$ mm^3, and the number of voxels is $15 \times 15 \times 10$. The values of the azimuth and elevation angles are 0° and 90° for 2D images and for 3D images 37.5° and 30°, respectively. The tissue phantoms were reconstructed using the perturbation data obtained as a difference between the rCWDOT's measurements acquired from the tail fat with and without spleen inside it. The shape of the spleen was spherical approximately. The spleen dimensions were approximately 0.5 cm in x, y, and z directions. Spleen tissues were first placed in the depth of 0.5 cm and then 1 cm inside the tail fat. The phantom images with a spleen at approximately 0.5 and 1 cm depths are shown in Figures 4 and 5, respectively. PSNR values before and after image processing are 6.9255 and 17.7082, respectively.

Figure 5 shows that the reconstructed image through the x–y, x–z, and x–y–z planes for the spleen was placed at $x = 1.75$ cm, $y = 1.25$ cm, and $z = 1$ cm. Figure 5(A) displays the raw image through the x–y plane. Figure 5(B) shows the processed image in the x–y plane. Figure 5(C,D) displays the raw and processed images in the x–z plane, respectively. Figure 5(E) shows the processed 3D image of the spleen. The location of the spleen in the 3D image is compatible with the spleen's actual location in the tail fat breast

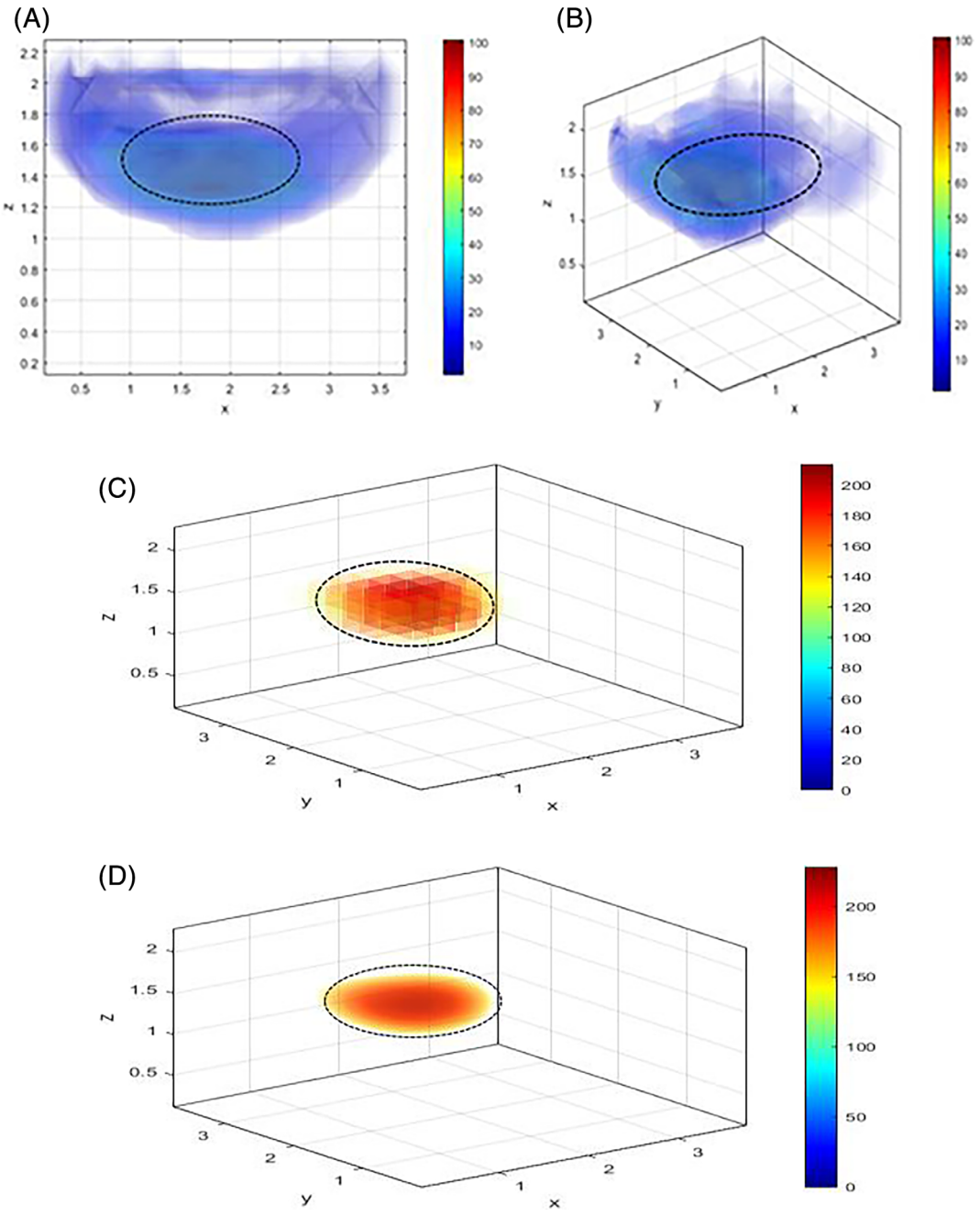

FIGURE 3 The test experiment, spatial coordinates of the spleen in tail fat at $x = 1.5$ cm, $y = 1.25$ cm, and $z = 1$ cm. The dashed line indicates the actual size and location of the spleen. (A) The reconstructed image through the x–z plane 2D image. (B) The x–y–z plane 3D image. (C) 3D image after Gaussian filtering. (D) 3D image after Gaussian filtering and bi-cubic interpolation. The color bars represent the intensity of absorption and x–y–z coordinate units in centimeters for all figures

phantom. PSNR values before and after image processing are 7.6029 and 16.6358, respectively.

Figure 6 shows that the raw and processed images through the x–y, x–z, and x–y–z planes for the spleen tissue were placed diagonally in the x–y plane at a depth of approximately 0.75 cm. The length and diameter of the spleen were approximately 2 and 0.5 cm, respectively. Figure 6(A) shows the raw image through the x–y plane, and Figure 6(B) shows the reconstructed image in the x–z plane. Figure 6(C,D) displays the raw and processed images in the x–z plane, respectively. Figure 6(E) shows the spleen tissue. PSNR values before and after image processing are 7.9318 and 16.9432, respectively.

The images obtained before and after the image processing of inclusion are shown in Figures 4–6. As a result, PSNR (in dB) values for all experimental images are calculated and listed below in Table 1.

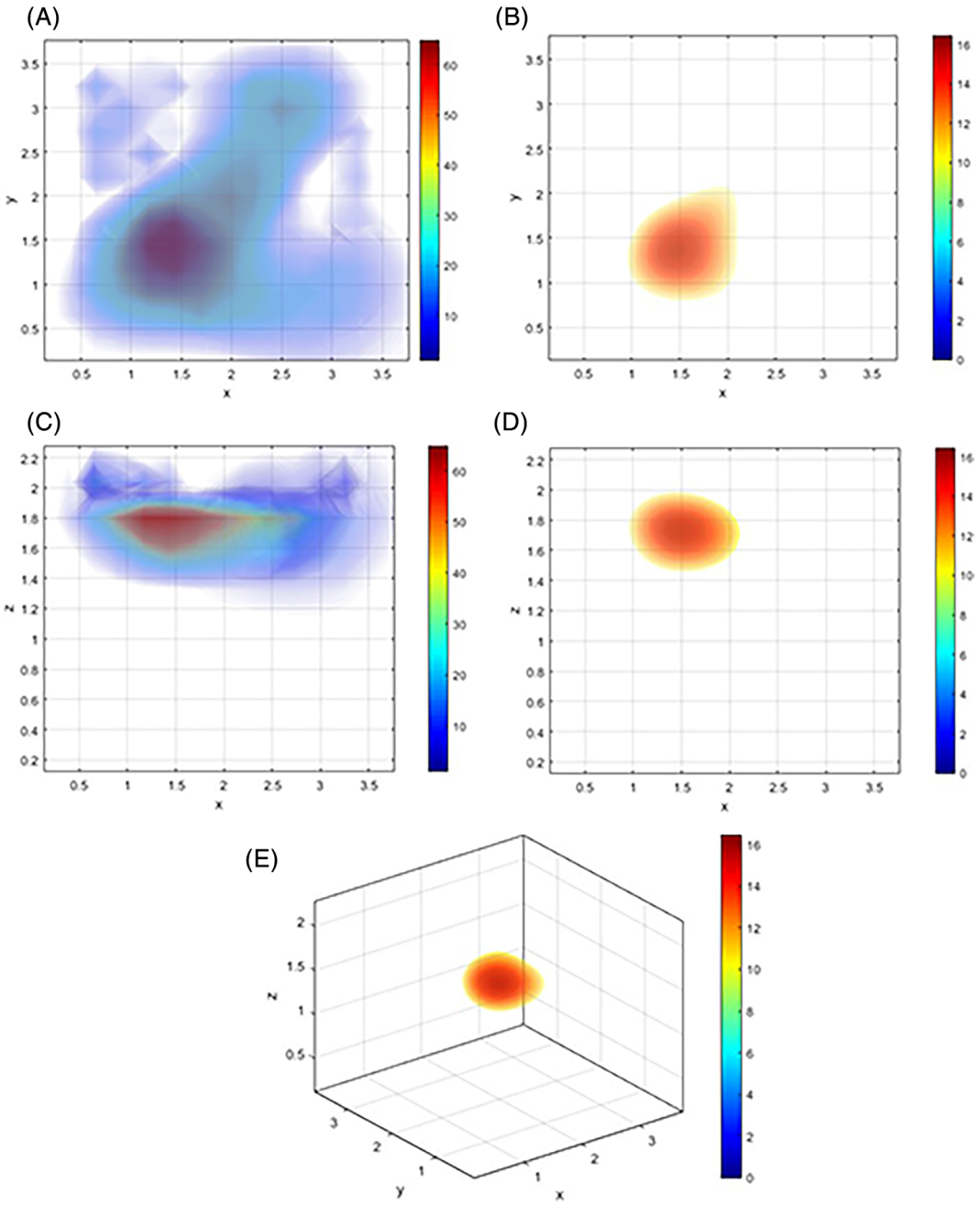

FIGURE 4 The spleen in tail fat at $x = 1.5$ cm, $y = 1.25$ cm, and $z = 0.5$ cm. (A) The reconstructed image through the x–y plane 2D image. (B) The x–y plane 2D image after image processing. (C) The reconstructed 2D image through the x–z plane. (D) The x–z plane 2D image after image processing. (E) 3D image after image processing. The color bars represent the intensity of absorption and x–y–z coordinate units are centimeters for all figures. Image quality assessment PSNR = 6.9255 for (A) and (C); and PSNR = 17.7082 for (B), (D), and (E)

4 | DISCUSSION AND CONCLUSION

CG-typed reconstruction algorithms are the most effective iterative method to find a solution of a large, sparse, Hermitian, positive definite linear system; therefore, they are the most used reconstruction algorithms in rCWDOT (Guadette et al. 2000).[22,24,25,38] In our previous studies, we have investigated the most suitable reconstruction technique for the rCWDOT system by reconstructing homogenous tissue phantoms composed of a mixture of intralipid, pure-water, and indocyanine green.[21,22,39] Our previous study showed that the TFQMR reconstruction algorithm is better than the BiCG.[21,39] In the presented study, the rCWDOT data were acquired from the breast phantom with a heterogeneous structure that resembles the actual breast based on its fat content (Figure 1). In a tumor-like

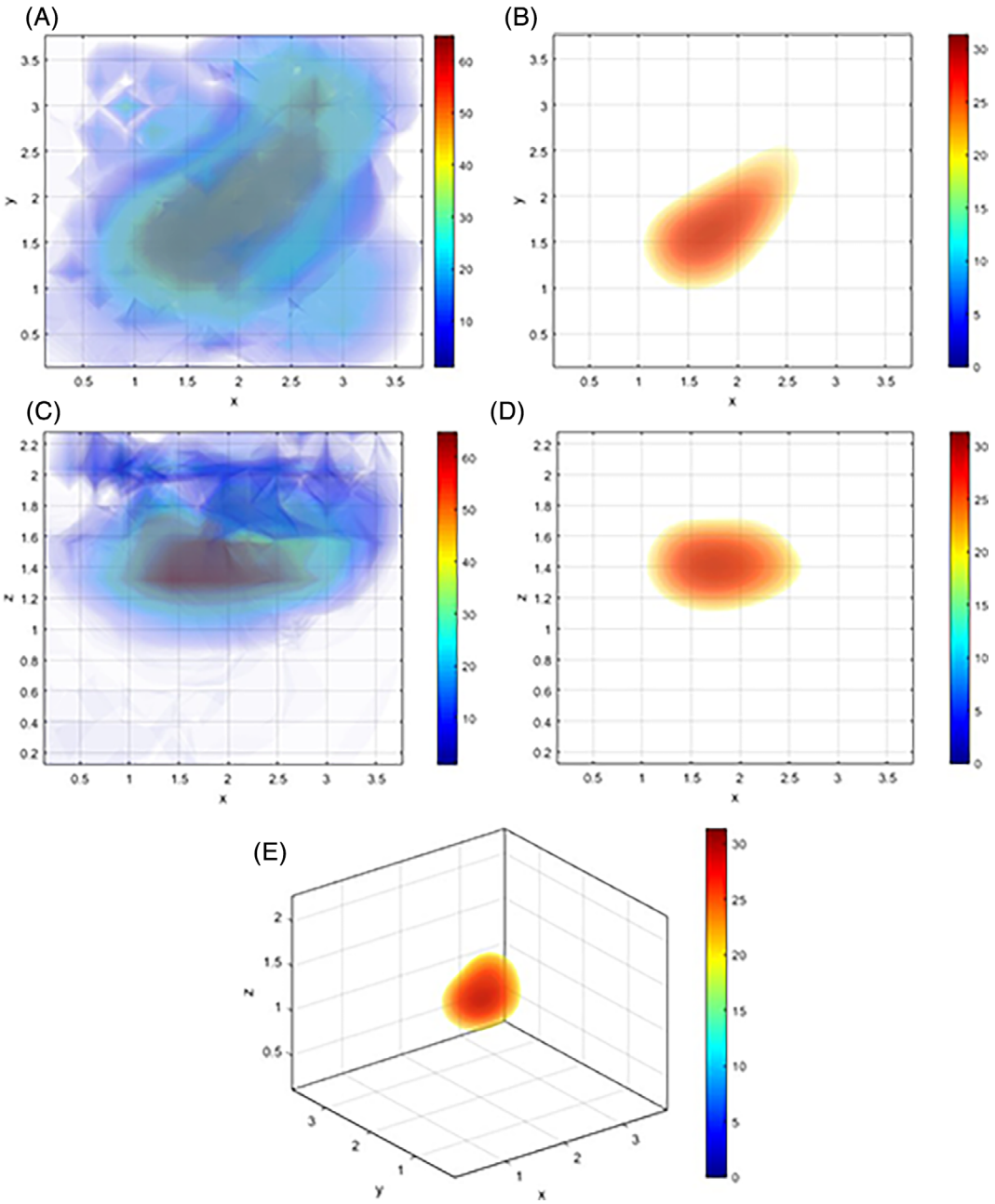

FIGURE 5 The spleen in tail fat at $x = 1.5$ cm, $y = 1.25$ cm, and $z = 1$ cm. (A) The reconstructed image through the x–y plane 2D image. (B) The x–y plane 2D image after image processing. (C) The reconstructed 2D image through the x–z plane. (D) The x–z plane 2D image after image processing. (E) 3D image after image processing. The color bars represent the intensity of absorption, and x–y–z coordinate units are centimeters for all figures. Image quality assessment PSNR = 7.6029 for (A) and (C); and PSNR = 16.6358 for (B), (D), and (E)

sample, a bit of spleen was inserted in tail fat to mimic the tumoral structure. The rCWDOT system was used to acquire data from tail fat without and with the spleen. After reconstructing the breast phantom by TFQMR and then image processing methods such as 3D Gaussian filtering and bi-cubic interpolation (Figure 2), the effectiveness of the image processing algorithms in removing noise from the images of heterogeneous breast phantoms has been shown (Figures 4–6(E)).

Proper improvements with image processing algorithms can minimize the noise in the images. In noisy data, the tumor-like structures are only barely visible in all 3D images. The 3D Gaussian filtering scheme reduces the noise in 3D reconstructed images.[26] Interpolation techniques determine the values of a function between

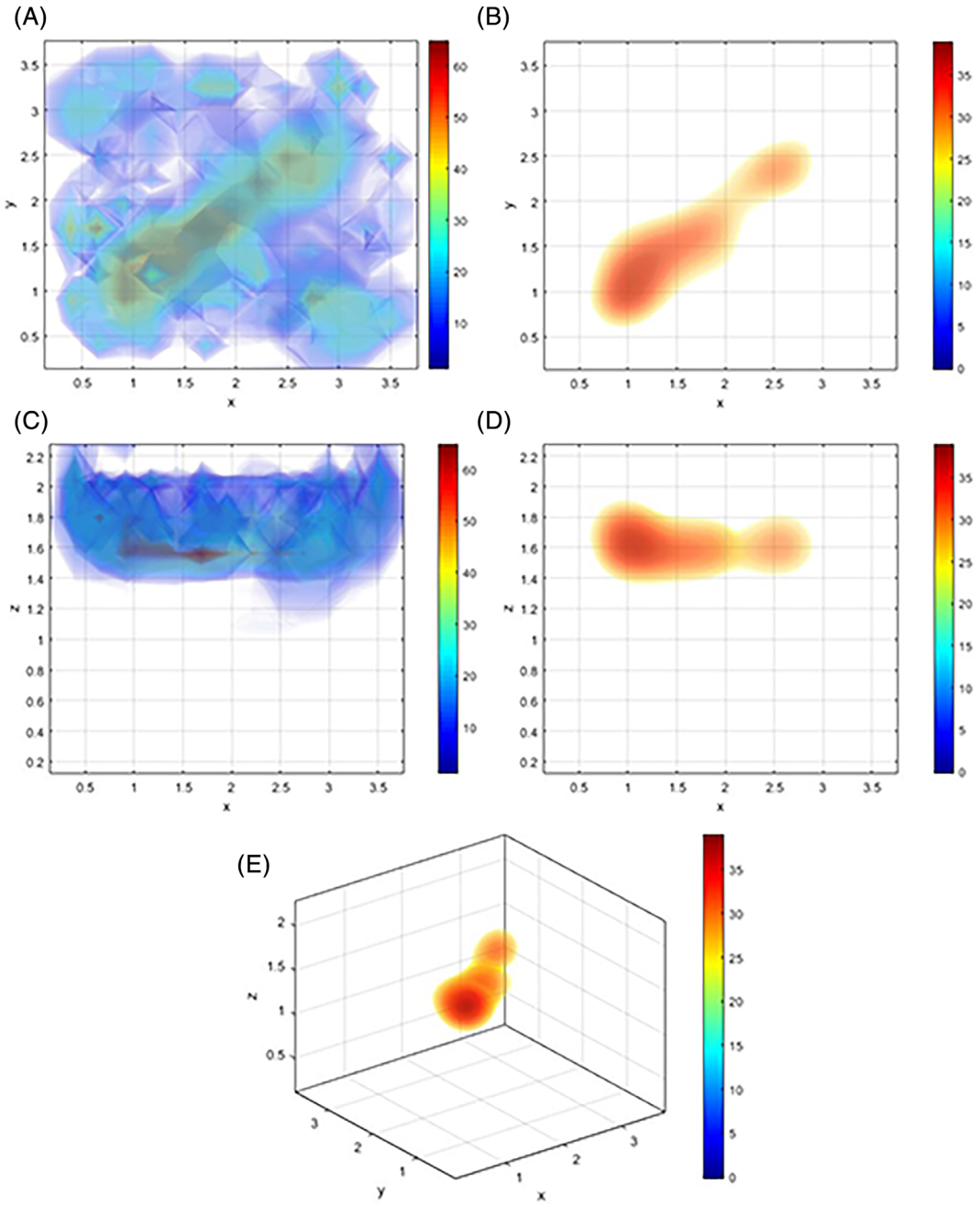

FIGURE 6 Images of the spleen length of 2 cm and diameter of 0.4 cm located diagonally in the *x*–*y* plane at a depth of 0.75 cm. (A) The reconstructed image through the *x*–*y* plane 2D image. (B) The *x*–*y* plane 2D image after image processing. (C) The reconstructed 2D image through the x-z plane. (D) The *x*–*z* plane 2D image after image processing. (E) 3D image after image processing. The color bars represent the intensity of absorption and *x*–*y*–*z* coordinate units are centimeters for all figures. Image quality assessment PSNR = 7.9318 for (A) and (C); and PSNR = 16.9432 for (B), (D), and (E)

its samples to increase the images' resolution. The quality of a processed image depends on the adapted interpolation technique. After the image processing, the calculated PSNR values provide to determine an improvement on the image.[27,28] We observed that the quality of the image improved according to the PSNR value presented in Table 1. A spleen tissue was used as a tumor-relevant similar structure located at three different depths of approximately 0.5, 0.75, and 1 cm (Figures 4–6). TFQMR correctly reconstructed the tumor-relevant similar structure at depths of approximately 0.5, 0.75, and 1 cm. Therefore, we conclude that TFQMR can accurately define the breast tumor's location up to 1 cm (Figure 6). Our results show that the implemented image processing algorithm reduces noise and allows the detection of lesions at different depths (Figures 4–6(B,D)) and shapes

TABLE 1 PSNR (in dB) values before and after image processing for all experiments

Figures	PSNR (in dB) results	
	Before image processing	After image processing
Figure 4	6.9255	17.7082
Figure 5	7.6029	16.6358
Figure 6	7.9318	16.9432

can be detected by the rCWDOT system (Figures 4–6(A,C)). The results have shown that the used image processing methods reduce noise while preserving the utility details of the image.

The proposed algorithms can be applied automatically, and the noise is suppressed well and the algorithms performed better in all images. Also, we have shown that better quality images can be obtained from optical imaging systems with fewer experimental errors by using image processing algorithms such as 3D Gaussian filtering and bi-cubic interpolation for the first time used in heterogeneous breast phantom images of the rCWDOT system. Thus, we have proved that the algorithm can be applied to the rCWDOT system and works properly. We can reveal the resolution between reconstructed and image processing by calculating PSNR. The results of PSNR are higher after image processing as shown in Table 1.

It is the advantage of TFQMR compared with other reconstruction techniques that need additional depth correction to find the lesion's correct location.[40–43] Since rCWDOT provides only absorption of the tissue along the optical path between the source and detector, the distribution of absorption was reconstructed. Therefore, only location and shape of the lesions were obtained rather than absorption's coefficient distribution, which is one of the limitations of the present study. One of the main results is to apply image processing algorithms such as Gaussian filtering and bi-cubic interpolation to improve quantization and noise suppression. It successfully described the border, location, and different shapes of the tumor-relevant similar structure within a heterogeneous medium similar to the breast tissue.

Our results show that the reconstruction and the image processing algorithms work not only for a spherical but also for tumor-relevant similar structure. Therefore, we conclude that TFQMR can be used in the rCWDOT system, as a reconstruction algorithm and Gaussian filtering, and bi-cubic interpolation as an image processing algorithm in in vivo studies to determine the shape and depth of the tumor. This study has shown that image processing algorithms have provided a better solution in rCWDOT images.

5 | FUTURE WORK

This study has shown that the image processing algorithms have provided a better solution in rCWDOT images. The future way for rCWDOT will contribute to researchers using our proposed image processing algorithms with reconstruction algorithms that will perform clinical experiments in this field.

ACKNOWLEDGMENTS

This work was supported in part by the Akdeniz Üniversitesi Scientific Research Project Council, Project No: 2009.02.0122.003, and in part by TUBITAK, Project No: 110E263.

CONFLICT OF INTEREST

The authors report no conflicts of interest. The authors alone are responsible for the content and writing of this article.

DATA AVAILABILITY STATEMENT

Data available on request from the authors.

ORCID

Yiğit Ali Üncü https://orcid.org/0000-0001-7398-9540
Gençay Sevim https://orcid.org/0000-0002-2157-3209
Murat Canpolat https://orcid.org/0000-0003-3298-9725

REFERENCES

1. Chae EY, Kim HH, Sabir S, et al. Development of digital breast tomosynthesis and diffuse optical tomography fusion imaging for breast cancer detection. *Sci Rep*. 2020;10(1):13127. https://doi.org/10.1038/s41598-020-70103-0
2. Dehghani H, Pogue BW, Poplack SP, Paulsen KD. Multi-wavelength three-dimensional near-infrared tomography of the breast: initial simulation, phantom, and clinical results. *Appl Opt*. 2003;42:135-145. https://doi.org/10.1364/AO.42.000135
3. Hebden JC, Veenstra H, Dehghani H, et al. Three-dimensional time-resolved optical tomography of a conical breast phantom. *Appl Opt*. 2001;40:3278-3287. https://doi.org/10.1364/AO.40.003278
4. McBride TO, Pogue BW, Poplack S, et al. Multispectral near-infrared tomography: a case study in compensating for water and lipid content in hemoglobin imaging of the breast. *J Biomed Opt*. 2002;7:72-79. https://doi.org/10.1117/1.1428290
5. Ntziachristos V, Hielscher AH, Yodh AG, Chance B. Diffuse optical tomography of highly heterogeneous media. *IEEE Trans Med Imaging*. 2001;20:470-478. https://doi.org/10.1109/42.929613
6. Brigadoi S, Powell S, Cooper RJ, et al. Evaluating real-time image reconstruction in diffuse optical tomography using

physiologically realistic test data. *Biomed Opt Express*. 2015;6:4719-4737. https://doi.org/10.1364/BOE.6.004719

7. Gibson AJ, Hebden JC, Arridge SR. Recent advances in diffuse optical imaging. *Phys Med Biol*. 2005;50:R1-R43. https://doi.org/10.1088/0031-9155/50/4/r01
8. Chow YT, Ito K, Liu K, Zou J. Direct sampling method for diffusive optical tomography. *SIAM J Sci Comput*. 2015;37:A1658-A1684. https://doi.org/10.1137/14097519X
9. Chuang CC, Tsai JC, Chen CM, Yu ZH, Sun CW. Convergence rate calculation of simultaneous iterative reconstruction technique algorithm for diffuse optical tomography image reconstruction: a feasibility study. *Opt Commun*. 2012;285:2236-2241. https://doi.org/10.1016/j.optcom.2011.12.042
10. Boas DA, Brooks DH, Miller EL, et al. Imaging the body with diffuse optical tomography. *IEEE Signal Process Mag*. 2001;18:57-75. https://doi.org/10.1109/79.962278
11. Deng B, Brooks DH, Boas DA, Lundqvist M, Fang Q. Characterization of structural-prior guided optical tomography using realistic breast models derived from dual-energy X-ray mammography. *Biomed Opt Express*. 2015;6:2366-2379. https://doi.org/10.1364/BOE.6.002366
12. Folkman J, Watson K, Ingber D, Hanahan D. Induction of angiogenesis during the transition from hyperplasia to neoplasia. *Nature*. 1989;339:58-61. https://doi.org/10.1038/339058a0
13. Ban HY, Busch DR, Pathak S, et al. Diffuse optical tomography in the presence of a chest wall. *J Biomed Opt*. 2013;18:026016. https://doi.org/10.1117/1.JBO.18.2.026016
14. Yodh A, Chance B. Spectroscopy and imaging with diffusing light. *Phys Today*. 1995;48:34-40. https://doi.org/10.1063/1.881445
15. Yuan Z, Zhang Q, Sobel ES, Jiang H. Image-guided optical spectroscopy in diagnosis of osteoarthritis: a clinical study. *Biomed Opt Express*. 2010;1:74-86. https://doi.org/10.1364/BOE.1.000074
16. Arridge SR. Optical tomography in medical imaging. *Inverse Probl*. 1999;15:R41-R93. https://doi.org/10.1088/0266-5611/15/2/022
17. Boas DA. A fundamental limitation of linearized algorithms for diffuse optical tomography. *Opt Express*. 1997;1:404-413. https://doi.org/10.1364/oe.1.000404
18. Durduran T, Choe R, Baker WB, Yodh AG. Diffuse optics for tissue monitoring and tomography. *Rep Prog Phys*. 2010;73:076701. https://doi.org/10.1088/0034-4885/73/7/076701
19. Haskell RC, Svaasand LO, Tsay TT, Feng TC, Tromberg BJ, McAdams MS. Boundary conditions for the diffusion equation in radiative transfer. *J Opt Soc Am A*. 1994;11:2727-2741. https://doi.org/10.1364/josaa.11.002727
20. Hoshi Y, Yamada Y. Overview of diffuse optical tomography and its clinical applications. *J Biomed Opt*. 2016;21:091312. https://doi.org/10.1117/1.jbo.21.9.091312
21. Sevim G, Üncü YA, Mercan T, Canpolat M. Image reconstruction for diffuse optical tomography using bi-conjugate gradient and transpose-free quasi minimal residual algorithms and comparison of them. *Int J Imaging Syst Technol*. 2021;6(4):297-304. https://doi.org/10.1002/ima.22587
22. Mercan T, Sevim G, Üncü YA, Serkan USLU, Kazanci HÖ, Canpolat M. The comparison of reconstruction algorithms for diffuse optical tomography. *Süleyman Demirel Üniversitesi Fen Edebiyat Fakültesi Fen Dergisi*. 2019;14(2):285-295. https://doi.org/10.29233/sdufeffd.549528
23. Gaudette RJ, Brooks DH, DiMarzio CA, et al. A comparison study of linear reconstruction techniques for diffuse optical tomographic imaging of absorption coefficient. *Phys Med Biol*. 2000;45:1051-1070. https://doi.org/10.1088/0031-9155/45/4/318
24. Gutknecht MH. A brief Introduction to Krylov space methods for solving linear systems. *Front Comput Sci*. In: *Frontiers of Computational Science*, Berlin, Heidelberg: Springer; 2007;53–62. https://doi.org/10.1007/978-3-540-46375-7_5
25. Liesen, J. and Strakos, Z. (2013), *Krylov Subspace Methods: Principles and Analysis*, Oxford Scholarship Online: Oxford University Press. https://doi.org/10.1093/acprof:oso/9780199655410.001.0001.
26. Zhang XH, Ning R, Yang D. Cone beam breast CT noise reduction using 3D adaptive Gaussian filtering. *J Xray Sci Technol*. 2009;17:319-333. https://doi.org/10.3233/XST-2009-0232
27. Lehmann TM, Gönner C, Spitzer K. Survey: interpolation methods in medical image processing. *IEEE Trans Med Imaging*. 1999;18:1049-1075. https://doi.org/10.1109/42.816070
28. Leng J, Xu G, Zhang Y. Medical image interpolation based on multi-resolution registration. *Comput Math Appl*. 2003;66:1-18. https://doi.org/10.1016/j.camwa.2013.04.026
29. Achim A, Bezerianos A, Tsakalides P. Novel Bayesian multiscale method for speckle removal in medical ultrasound images. *IEEE Trans Med Imaging*. 2001;20:772-783. https://doi.org/10.1109/42.938245
30. DiFrancesco MW, Rasmussen JM, Yuan W, et al. Comparison of SNR and CNR for in vivo mouse brain imaging at 3 and using well matched scanner configurations. *Med Phys*. 2008;35:3972-3978. https://doi.org/10.1118/1.2968092
31. Mateo JL, Fernández-Caballero A. Finding out general tendencies in speckle noise reduction in ultrasound images. *Expert Syst Appl*. 2009;36:7786-7797. https://doi.org/10.1016/j.eswa.2008.11.029
32. Robson PM, Grant AK, Madhuranthakam AJ, Lattanzi R, Sodickson DK, McKenzie CA. Comprehensive quantification of signal-to-noise ratio and g-factor for image-based and k-space-based parallel imaging reconstructions. *Magn Reson Med*. 2008;60:895-907. https://doi.org/10.1002/mrm.21728
33. Canpolat M, Kazanci HÖ, Mercan T, Alimoğlu E. Design of breast laser tomography system and pilot clinical results. *Akdeniz Med J*. 2015;1(1):58-63. https://doi.org/10.17954/amj.2015.07
34. Kazanci HÖ, Mercan T, Canpolat M. Design and evaluation of a reflectance diffuse optical tomography system. *Opt Quant Electron*. 2014;47:257-265. https://doi.org/10.1007/s11082-014-9910-6
35. Üncü YA, Sevim G, Mercan T, Vural V, Durmaz E, Canpolat M. Differentiation of tumoral and non-tumoral breast lesions using back reflection diffuse optical tomography: a pilot clinical study. *Int J Imaging Syst Technol*. 2021. https://doi.org/10.1002/ima.22578.
36. Freund RW. A transpose-free quasi-minimal residual algorithm for non-Hermitian linear systems. *SIAM J Sci Comput*. 1993;14:470-482. https://doi.org/10.1137/0914029
37. Freund RW. Transpose-free quasi-minimal residual methods for non-Hermitian linear systems. In: Golub G, Luskin M, Greenbaum A, eds. *Recent Advances in Iterative Methods*. The IMA Volumes in Mathematics and its Applications; New York:

Springer; 1994:69–94. https://doi.org/10.1007/978-1-4613-9353-5_6

38. Mercan, T., Sevim G, Kazancl H.Ö, Üncü Y.A, Canpolat M. (2017) 'Comparison of images produced by diffuse optical tomography with two different backscatter techniques. Proceedings of the 2017 21st National Biomedical Engineering Meeting (BIYOMUT). https://doi.org/10.1109/BIYOMUT.2017.8479038.
39. Sevim, G. (2017) A new reconstruction technique used in diffuse optical tomography system. Proceedings of the 2017 21st National Biomedical Engineering Meeting (BIYOMUT). doi: https://doi.org/10.1109/BIYOMUT.2017.8478965.
40. Bhowmik T, Liu H, Ye Z, Oraintara S. Dimensionality reduction based optimization algorithm for sparse 3-D image reconstruction in diffuse optical tomography. *Sci Rep*. 2016;6(1):1-13. https://doi.org/10.1038/srep22242
41. Niu H, Tian F, Lin ZJ, Liu H. Development of a compensation algorithm for accurate depth localization in diffuse optical tomography. *Opt Lett*. 2010;2010:429-431. https://doi.org/10.1364/OL.35.000429
42. Niu H, Lin Z, Tian F, Dhamne S, Liu H. Comprehensive investigation of three-dimensional diffuse optical tomography with depth compensation algorithm. *J Biomed Opt*. 2010;15(4):046005. https://doi.org/10.1117/1.3462986
43. Tian FH, Niu H, Khadka S, Lin ZJ, Liu H. Algorithmic depth compensation improves quantification and noise suppression in functional diffuse optical tomography. *Biomed Opt Express*. 2010;1(2):441-452. https://doi.org/10.1364/BOE.1.000441

How to cite this article: Üncü YA, Sevim G, Canpolat M. Approaches to preclinical studies with heterogeneous breast phantom using reconstruction and three-dimensional image processing algorithms for diffuse optical imaging. *Int J Imaging Syst Technol*. 2021;1-11. doi: 10.1002/ima.22648